Micromotion minimization using Ramsey interferometry

New Journal of Physics
The open access journal at the forefront of physics

Deutsche Physikalische Gesellschaft DPG IOP Institute of Physics

Micromotion minimization using Ramsey interferometry

To cite this article: Gerard Higgins *et al* 2021 *New J. Phys.* **23** 123028

New Journal of Physics
The open access journal at the forefront of physics

Deutsche Physikalische Gesellschaft DPG
IOP Institute of Physics

Published in partnership with: Deutsche Physikalische Gesellschaft and the Institute of Physics

OPEN ACCESS

RECEIVED
16 July 2021

REVISED
15 October 2021

ACCEPTED FOR PUBLICATION
26 November 2021

PUBLISHED
16 December 2021

PAPER

Micromotion minimization using Ramsey interferometry

Gerard Higgins[1,2,3,*], **Shalina Salim**[1], **Chi Zhang**[1,4], **Harry Parke**[1], **Fabian Pokorny**[1,5] and **Markus Hennrich**[1]

[1] Department of Physics, Stockholm University, Stockholm, Sweden
[2] Department of Microtechnology and Nanoscience, Chalmers University of Technology, Gothenburg, Sweden
[*] Author to whom any correspondence should be addressed.
[3] Present address: Institute for Quantum Optics and Quantum Information (IQOQI), Austrian Academy of Sciences, Vienna, Austria.
[4] Present address: Centre for Cold Matter, Imperial College London, London, United Kingdom.
[5] Present address: Department of Physics, University of Oxford, Oxford, United Kingdom.

E-mail: higgins@chalmers.se

Keywords: trapped ion micromotion, Paul trap, clock synchronization, Ramsey interferometry, quantum metrology, micromotion minimization

Supplementary material for this article is available online

Abstract

We minimize the stray electric field in a linear Paul trap quickly and accurately, by applying interferometry pulse sequences to a trapped ion optical qubit. The interferometry sequences are sensitive to the change of ion equilibrium position when the trap stiffness is changed, and we use this to determine the stray electric field. The simplest pulse sequence is a two-pulse Ramsey sequence, and longer sequences with multiple pulses offer a higher precision. The methods allow the stray field strength to be minimized beyond state-of-the-art levels. Using a sequence of nine pulses we reduce the 2D stray field strength to (10.5 ± 0.8) mV m^{-1} in 11 s measurement time. The pulse sequences are easy to implement and automate, and they are robust against laser detuning and pulse area errors. We use interferometry sequences with different lengths and precisions to measure the stray field with an uncertainty below the standard quantum limit. This marks a real-world case in which quantum metrology offers a significant enhancement. Also, we minimize micromotion in 2D using a single probe laser, by using an interferometry method together with the resolved sideband method; this is useful for experiments with restricted optical access. Furthermore, a technique presented in this work is related to quantum protocols for synchronizing clocks; we demonstrate these protocols here.

1. Introduction

In a Paul trap ions are confined using an oscillating electric quadrupole field. Ideally the equilibrium position of a single trapped ion will coincide with the null of the oscillating quadrupole field. Stray electric fields as well as trap fabrication imperfections introduce a quasi-static dipole electric field **E** at the null of the oscillating quadrupole field, which displaces the ion equilibrium position from the oscillating field null. This results in an oscillating dipole field at the ion equilibrium position, which drives oscillatory ion motion, called excess micromotion [1].

The oscillating dipole field causes a Stark shift and the excess micromotion causes a Doppler shift, both effects impact precision spectroscopy [2], and the Stark shifts are particularly troublesome in experiments using highly-polarizable Rydberg ions [3, 4]. Furthermore, the energy stored in excess micromotion is an obstacle to studies of quantum interactions in hybrid systems of neutral atoms and trapped ions [5–8]. The Stark shift and the excess micromotion can be diminished by applying a static electric dipole field to counter the unwanted quasi-static dipole field **E**. This opposing electric field is usually produced by applying voltages to dedicated compensation electrodes.

Although a host of techniques have been developed to determine appropriate compensation electrode voltages [1–3, 8–23], there is a demand to improve upon the existing techniques, so that trapped ions can

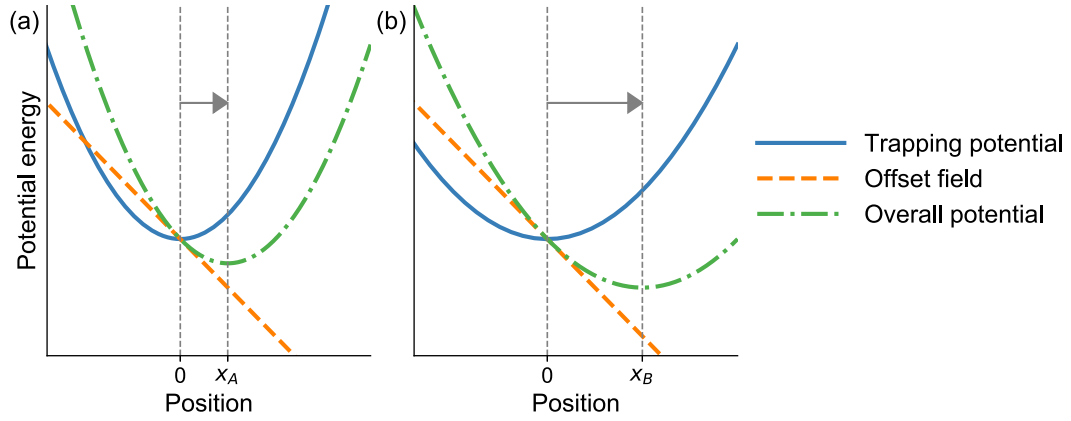

Figure 1. At the minimum (position 0) of a Paul trap's effective RF potential (blue solid lines) there is no oscillating dipolar electric field. A static dipolar offset field **E** (corresponding to the orange dashed potential) displaces the trapping pseudopotential, causing an ion trapped at the displaced minimum (x_A in (a), x_B in (b)) to experience an oscillating dipolar electric field which drives excess micromotion. The offset field **E** is the same in both plots. The displacement from 0 is larger in (b) than in (a) because the trap stiffness is weaker in (b). By changing the trap stiffness and measuring the change of a trapped ion's position information is gained about **E** (see equation (2)).

be controlled ever more precisely. Some of the most popular methods for minimising excess micromotion rely on the impact of micromotion on an ion's absorption or emission spectra, through the Doppler effect [1, 2, 9–11]. For instance, micromotion introduces spectral sidebands which are separated from carrier transitions by the frequency of the trap's oscillating quadrupole field [1, 2]. It also modulates the ion's scattering rate at the frequency of the trap's oscillating quadrupole field [1, 2].

Other techniques rely on measuring the change of a trapped ion's equilibrium position when the trap stiffness is changed [1, 8, 12–14, 24]; the methods we present here also work in this fashion. These techniques are explained as follows: the unwanted quasi-static dipole field **E** at the position of the trap's oscillating field null displaces the equilibrium position of a trapped ion from the null by **r**, where [1]

$$r_i = \frac{qE_i}{m\omega_i{}^2} \tag{1}$$

and q is the ion charge, m is the ion mass, the three spatial directions indexed by i are defined by the ion's secular motion, and ω_i is the trap stiffness (the frequency of the trapping pseudopotential) in the i direction. When the trap stiffness is changed $\omega_{Ai} \rightarrow \omega_{Bi}$ the ion equilibrium position is displaced by $\mathbf{r}_{AB}$, which has the components

$$r_{ABi} = \frac{qE_i}{m}\left(\frac{1}{\omega_{Bi}{}^2} - \frac{1}{\omega_{Ai}{}^2}\right). \tag{2}$$

This is represented in figure 1.

By measuring effects sensitive to $\mathbf{r}_{AB}$ ion trappers gain information about **E**. The displacement $\mathbf{r}_{AB}$ is commonly monitored by imaging a trapped ion [1, 8, 12, 13, 24]. It can also be detected by measuring the strength with which transitions are driven when there is an optical field gradient [14] or a magnetic field gradient [8]. These methods are limited by the imaging resolution, by optical diffraction limits and laser powers, and by achievable magnetic field gradients respectively.

In this work we use interferometry to measure $\mathbf{r}_{AB}$ with a resolution much less than an optical wavelength. This allows us to reduce $|\mathbf{E}|$ beyond state-of-the-art levels in a short time, and thereby diminish excess micromotion. We apply different Ramsey-interferometry pulse sequences to a single trapped ion to probe $\mathbf{r}_{AB}$. Using a sequence of two $\pi/2$ pulses resonant to an optical transition we determine the projection of $\mathbf{r}_{AB}$ along one direction with resolution $\approx\frac{\lambda}{2\pi\sqrt{N}}$, where λ is the wavelength of the laser field and N is the number of experimental cycles. We improve on this resolution using sequences of $M+1$ coherent pulses, which offer an M-fold precision enhancement. The pulse sequences are described in section 2.

In section 3 we demonstrate fast and accurate minimization of **E**, and discuss the impact that changing the RF power supplied to the trap has on the trap temperature.

In section 4 we show that by conducting interferometry pulse sequences of different lengths $\mathbf{r}_{AB}$ and **E** can be probed with an uncertainty below the standard quantum limit. The pulse sequences can be designed so that the results are robust against pulse area errors and laser detuning; we demonstrate this in section 5.

In section 6 we apply the methods to minimize micromotion in 2D and 3D. We also demonstrate 2D micromotion minimization using just a single laser beam, by using the interferometry method together with the commonly-used resolved sideband technique [1].

As well as enabling micromotion minimization, one of the pulse sequences presented here demonstrates clock-synchronization protocols which involve exchange of a ticking qubit [25, 26]. This is described in section 7.

2. Pulse sequences

In this section we present methods to minimize $|\mathbf{E}|$ using interferometry sequences, but first we introduce some key concepts: the action of a sequence of laser pulses on a transition $|g\rangle \leftrightarrow |e\rangle$ between two states of an ion can be described by a sequence of rotations on the Bloch sphere spanned by $|g\rangle$ and $|e\rangle$. When the laser field driving the pulses is resonant to the $|g\rangle \leftrightarrow |e\rangle$ transition, the rotation axes lie on the Bloch sphere's equator. The phase of the laser field during each pulse, within the ion's rotating frame, determines the azimuthal angle of each rotation axis.

Within the ion's rotating frame, the phase of the laser field is fixed in time (unless a controlled phase shift is introduced), and it varies in space according to

$$\Phi_{\alpha A} = \mathbf{k}_\alpha \cdot \mathbf{r}_A + \Phi_{\alpha 0}, \tag{3}$$

where $\mathbf{k}_\alpha$ is the wavevector of the laser field, $\Phi_{\alpha 0}$ is a constant phase offset, and Greek letters are used to index different laser beams along different directions while Roman letters are used to index different trap stiffness settings and the corresponding ion positions. The laser phase experienced by the ion depends on the ion position. This means the rotation axis of a laser pulse and the impact the pulse has on the ion's state also depend on the ion's position. By applying a sequence of pulses and measuring the ion's state we can probe the change of ion position $\mathbf{r}_{AB}$ when the trap stiffness is changed from setting $A \rightarrow B$.

We use Ramsey pulse sequences, comprising two $\pi/2$ pulses, as well as longer sequences with several π pulses between two $\pi/2$ pulses. In general the sequences comprise $M+1$ pulses and have pulse areas $M\pi$, where M is an integer and $M \geqslant 1$.

During the pulse sequences the phase of the laser field at the ion position is changed between pulses. This is accomplished by changing the phase of the laser beam which drives the pulse, or by using a different laser beam from a different direction, or by moving the ion from one position to another. We write the laser phase experienced by the ion during the jth pulse as $\phi_j + \theta_j$, where ϕ_j depends on both the ion position and the laser beam used to drive the pulses according to equation (3), while the controlled shift θ_j results from adding a phase shift to the laser field, using, for example, an acousto-optical modulator. $\{\phi_j\}$ are general phases, later we will substitute in specific phases using equation (3). If the ion is initially in state $|g\rangle$, after applying the pulse sequence the probability of measuring the ion in state $|e\rangle$ is

$$p = \frac{1}{2}\left[1 + \cos\left(\phi_{\mathrm{T}} + \theta_{\mathrm{T}}\right)\right], \tag{4}$$

where

$$\phi_{\mathrm{T}} = \phi_1 + 2\sum_{j=2}^{M}(-1)^{j-1}\phi_j + (-1)^M\phi_{M+1} \tag{5}$$

$$\theta_{\mathrm{T}} = \theta_1 + 2\sum_{j=2}^{M}(-1)^{j-1}\theta_j + (-1)^M\theta_{M+1} + \xi_M, \tag{6}$$

and where $\xi_M = \pi(0)$ if M is even (odd). The phase ϕ_{T} reveals information about the ion position, or change of position. By repeatedly applying the sequence and measuring the state of the ion, the probability p can be estimated, from which ϕ_{T} can be estimated (the controlled phase shift θ_{T} is known). An estimate of ϕ_{T} using a single p estimate and equation (4) is sensitive to pulse area errors and decoherence. More robust estimates of ϕ_{T} use two measurements of p using two different θ_{T} values. One can use [27]

$$\phi_{\mathrm{T}} = \arcsin\frac{p\left(\theta_{\mathrm{T}} = -\frac{\pi}{2}\right) - p\left(\theta_{\mathrm{T}} = \frac{\pi}{2}\right)}{\mathcal{C}\left[p\left(\theta_{\mathrm{T}} = -\frac{\pi}{2}\right) + p\left(\theta_{\mathrm{T}} = \frac{\pi}{2}\right)\right]}, \tag{7}$$

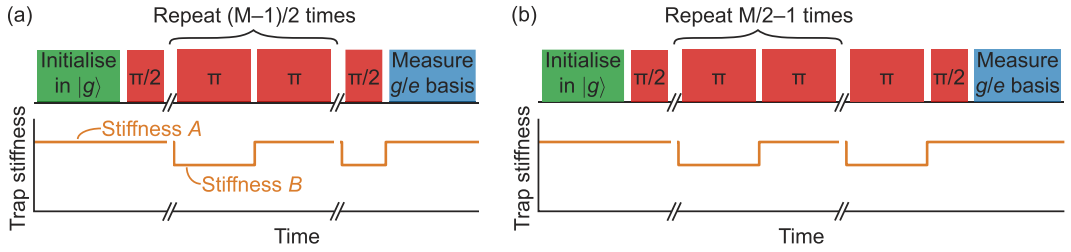

Figure 2. Method A involves a sequence in which the trap stiffness is changed between each coherent laser pulse. If there is an unwanted field **E**, changing the trap stiffness causes the ion to change position and experience a different laser phase. The probability of measuring the ion in $|e\rangle$ depends on the laser phases during the pulses, and thus on **E**. The areas of the coherent pulses (red) are indicated. The sequences in (a) and (b) are used when M is odd and even respectively. The shortest sequence is a Ramsey sequence with $M = 1$.

where $\mathcal{C}$ accounts for reduction of the contrast of the oscillation in equation (4), or one can use the two-argument arctangent function [28]

$$\phi_{\mathrm{T}} = \arctan 2\left[p\left(\theta_{\mathrm{T}} = -\frac{\pi}{2}\right) - \frac{1}{2}, p(\theta_{\mathrm{T}} = 0) - \frac{1}{2}\right] \tag{8}$$

Equation (7) performs well when $\phi_{\mathrm{T}} \approx 0$, and returns an estimate within a range of π, while equation (8) returns an estimate of ϕ_{T} within a range of 2π. When N experimental runs are conducted, $\frac{N}{2}$ using each value of θ_{T}, the statistical uncertainties of the ϕ_{T} estimates are $\approx\frac{1}{\sqrt{N}}$; the statistical uncertainties depend on the magnitude of ϕ_{T}, as shown in the supplemental material (https://stacks.iop.org/NJP/23/123028/mmedia) [29].

Pulse area errors and detuning of the laser field from resonance introduce systematic errors to estimates of ϕ_{T}. Systematic errors can be reduced by appropriately choosing the control phases $\{\theta_j\}$, as shown in section 5.

The pulse sequences presented here build on the sequence presented in reference [28]. In method A the coherent pulses are driven using a single laser beam and the trap stiffness is changed between pulses. In method B two laser beams are used and the trap stiffness is not changed between coherent pulses. In the supplemental material [29] we describe method C, which involves multiple laser beams with trap stiffness changes between the pulses.

2.1. Method A: sequence using a single laser beam

In the first method the laser pulses are driven by a single laser beam and the trap stiffness is alternated between stiffness A and stiffness B between laser pulses. The sequence is presented in figure 2. The trap stiffness changes cause the ion position to alternate between two positions, $\mathbf{r}_A$ and $\mathbf{r}_B$, and the position-dependent phase ϕ_j alternates between two values $\Phi_{\alpha A}$ and $\Phi_{\alpha B}$. Using equation (3), the difference between the phase values is

$$\Phi_{\alpha A} - \Phi_{\alpha B} = \mathbf{k}_\alpha \cdot (\mathbf{r}_A - \mathbf{r}_B) \tag{9}$$

and from equations (5) and (2)

$$\phi_{\mathrm{T}} = M\left(\Phi_{\alpha A} - \Phi_{\alpha B}\right) \tag{10}$$

$$= M\mathbf{k}_\alpha \cdot (\mathbf{r}_A - \mathbf{r}_B) \tag{11}$$

$$= M\sum_i \frac{qk_{\alpha i}E_i}{m}\left(\frac{1}{{\omega_{Ai}}^2} - \frac{1}{{\omega_{Bi}}^2}\right). \tag{12}$$

From equation (11) we see ϕ_{T} reveals the change in equilibrium position along the direction of $\mathbf{k}_\alpha$, and from Equation (12) we see ϕ_{T} is sensitive to **E** along the direction **d**, which has the components

$$d_i = k_{\alpha i}\left(\frac{1}{{\omega_{Ai}}^2} - \frac{1}{{\omega_{Bi}}^2}\right). \tag{13}$$

Thus, by probing and minimizing ϕ_{T}, the component of **E** along **d** can be minimized.

For convenience we define $\phi_{\mathrm{PD}} \equiv \Phi_{\alpha A} - \Phi_{\alpha B}$; the phase difference ϕ_{PD} depends on the path length difference from the laser source to $\mathbf{r}_A$ and from the laser source to $\mathbf{r}_B$. From equations (4), (10) and (12)

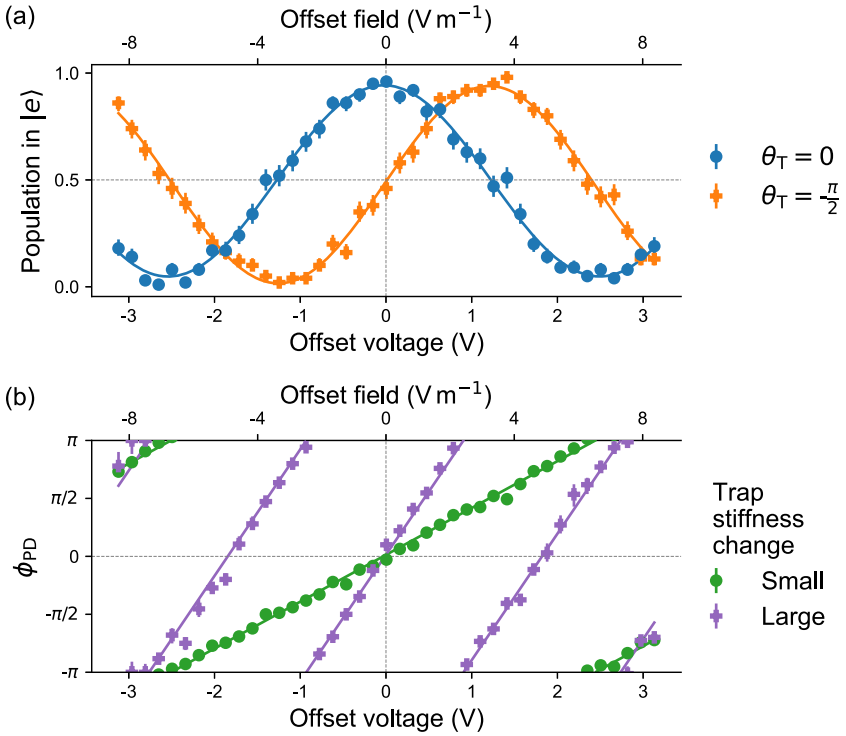

Figure 3. Micromotion minimization using method A. (a) The population measured in $|e\rangle$ depends sinusoidally on the offset voltage applied to a micromotion compensation electrode and the offset field strength. (b) The phase difference ϕ_{PD} depends linearly on the offset voltage, and is zero when micromotion is minimized. The green small-stiffness-change dataset was calculated from the datasets in (a) using equation (8). ϕ_{PD} responds more strongly to the offset field when the trap stiffness is changed by a larger amount. The solid lines in (a) and (b) are respectively sinusoidal and linear fits to the data. Error bars represent quantum projection noise (1σ confidence interval). The error bars are often smaller than the marker size.

$$p = \frac{1}{2}\left[1 + \cos\left(M\phi_{\mathrm{PD}} + \theta_{\mathrm{T}}\right)\right] \tag{14}$$

$$= \frac{1}{2}\left\{1 + \cos\left[M\sum_i \frac{qk_{\alpha i}E_i}{m}\left(\frac{1}{{\omega_{Ai}}^2} - \frac{1}{{\omega_{Bi}}^2}\right) + \theta_{\mathrm{T}}\right]\right\}. \tag{15}$$

With increasing M the precision of a ϕ_{PD} estimate is improved, at the expense of reducing the range within which ϕ_{PD} can be determined. ϕ_{PD} can be efficiently determined with a Heisenberg scaling by conducting measurements using different values of M; this is discussed further in section 4.

We experimentally demonstrate the workings of this method using a single $^{88}Sr^{+}$ ion confined in a linear Paul trap. A 674 nm laser field couples a Zeeman sublevel of the $5^2S_{1/2}$ ground state $|g\rangle$ with a Zeeman sublevel of the metastable $4^2D_{5/2}$ state $|e\rangle$. To initialise the ion in $|g\rangle$ we employ Doppler cooling as well as optical pumping on a transition between $5^2S_{1/2}$ and $4^2D_{5/2}$ sublevels. In some experiments we also employ sideband cooling. State detection involves probing the ion with 422 nm laser light near-resonant to the $5^2S_{1/2} \leftrightarrow 5^2P_{1/2}$ transition. The trap stiffness is changed between the laser pulses by changing the amplitude of the RF signal applied to the trap electrodes and thus changing the amplitude of the trap's oscillating quadrupole field. The electronics are described in detail in the supplemental material [29].

A component of $\mathbf{E}$ is varied by changing the voltage applied to a compensation electrode, and the effect on p is measured in a two-pulse Ramsey sequence ($M = 1$). The results are shown in figure 3(a). As expected from equation (15) p shows a sinusoidal dependence on the changes made to $\mathbf{E}$.

Figure 3(a) shows p values when two different values of θ_{T} were used. From this data and using equation (8) ϕ_{PD} was calculated; the results are shown in figure 3(b). The figure shows that ϕ_{PD} has a linear dependence on a component of $\mathbf{E}$, and that $\phi_{\mathrm{PD}} = 0$ when the compensation electrode offset voltage is zero. The point where the offset voltage is zero was independently determined using the resolved sideband technique [1]. Throughout this work compensation electrode offset voltages are shown relative to the optimal values as determined using the resolved sideband method.

The figure also shows the linear dependence of ϕ_{PD} on a component of $\mathbf{E}$ is stronger when the change of the trap stiffness is larger, as expected from the $({\omega_{Ai}}^{-2} - {\omega_{Bi}}^{-2})$ term in equation (12). The measurements involved reducing the radial secular frequencies from $\sim 2\pi \times 1.5$ MHz to $\sim 2\pi \times 600$ kHz for the green

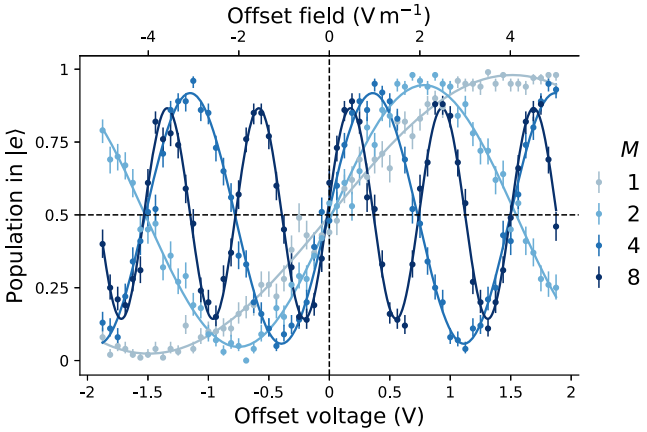

Figure 4. Method A becomes more sensitive to the compensation electrode offset voltage and to the offset field **E** with increasing sequence length M. Solid lines represent sinusoidal fits to the data. The oscillation contrast decreased as M was increased due to the short coherence time of our system. The $M = 2$ dataset had a negative gradient at zero offset voltage because it was measured with $\theta_{\mathrm{T}} = \frac{\pi}{2}$ while the other measurements used $\theta_{\mathrm{T}} = -\frac{\pi}{2}$; for better comparison of the datasets in the figure we have inverted the x-axis of the $M = 2$ dataset. Error bars represent quantum projection noise (1σ confidence interval).

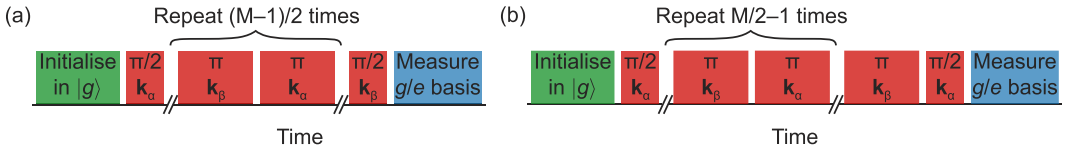

Figure 5. Method B involves coherent pulse sequences in which alternate pulses are driven by two different laser beams (with wavevectors $\mathbf{k}_\alpha$ and $\mathbf{k}_\beta$), while the trap stiffness is fixed. The probability of measuring the ion in $|e\rangle$ reveals the phase difference between the laser fields at the ion position. We measure the phase differences ϕ^A_{PD} and ϕ^B_{PD} at the ion equilibrium positions $\mathbf{r}_A$ and $\mathbf{r}_B$ when two different trap stiffness settings (A and B) are used. The quantity $\phi^A_{\mathrm{PD}} - \phi^B_{\mathrm{PD}}$ depends on $\mathbf{r}_{AB}$ and **E**. The sequences in (a) and (b) are used when M is odd and even respectively. The shortest sequence is a Ramsey sequence with $M = 1$.

small-stiffness-change dataset and to $\sim 2\pi \times 400$ kHz for the purple large-stiffness-change dataset. The axial secular frequency was fixed $\sim 2\pi \times 1.0$ MHz. Because equation (15) is cyclic it is possible to achieve $\phi_{\mathrm{PD}} = 0$ when $|\mathbf{E}|$ is not minimized, as seen for the purple large-stiffness-change dataset near ± 2 V. To check that $|\mathbf{E}|$ is truly minimized, one can check that ϕ_{PD} remains zero when different trap stiffness changes are used.

The probability p of measuring the ion in $|e\rangle$ becomes more sensitive to ϕ_{PD}, and thus to a component of **E**, as the sequence length M is increased. To show this we measured the dependence of p on the compensation electrode offset voltage with sequences of different lengths M; the results are shown in figure 4. The oscillation contrast decreased with increasing M, due to the limited coherence time in our experiment (~ 500 μs [30]).

2.2. Method B: sequence using a fixed trap stiffness

In the sequence described in this section the trap stiffness is fixed while the coherent pulses are applied, and alternate pulses are driven by two different laser beams. This is represented in figure 5.

If the ion is at position $\mathbf{r}_A$ and alternate pulses are driven by two different laser beams, with wavevectors $\mathbf{k}_\alpha$ and $\mathbf{k}_\beta$, the phase ϕ_j alternates between two values $\Phi_{\alpha A}$ and $\Phi_{\beta A}$. Using equation (3), the difference between these phase values is

$$\Phi_{\alpha A} - \Phi_{\beta A} = \left(\mathbf{k}_\alpha - \mathbf{k}_\beta\right) \cdot \mathbf{r}_A + \Phi_{\alpha 0} - \Phi_{\beta 0}. \tag{16}$$

If the two laser beams are derived from the same source, the phase difference depends on the path length difference from the point where the beams are split to the ion position $\mathbf{r}_A$. For convenience, we define $\phi^A_{\mathrm{PD}} \equiv \Phi_{\alpha A} - \Phi_{\beta A}$. From equation (5)

$$\phi_{\mathrm{T}} = M\left(\Phi_{\alpha A} - \Phi_{\beta A}\right) \tag{17}$$

$$\phi_{\mathrm{T}} = M\phi^A_{\mathrm{PD}}. \tag{18}$$

If the sequence is conducted using the fixed trap stiffness B then

$$\phi_{\mathrm{T}} = M\left(\Phi_{\alpha B} - \Phi_{\beta B}\right) \tag{19}$$

$$= M\left[\left(\mathbf{k}_{\alpha} - \mathbf{k}_{\beta}\right)\cdot\mathbf{r}_{B} + \Phi_{\alpha 0} - \Phi_{\beta 0}\right] \tag{20}$$

$$= M\phi^{B}_{\mathrm{PD}}, \tag{21}$$

where $\phi^{B}_{\mathrm{PD}} \equiv \Phi_{\alpha B} - \Phi_{\beta B}$. By conducting the sequence using each of the two trap stiffness settings, the phases ϕ^{A}_{PD} and ϕ^{B}_{PD} can be estimated, and therefrom the quantity

$$\phi^{A}_{\mathrm{PD}} - \phi^{B}_{\mathrm{PD}} = \left(\mathbf{k}_{\alpha} - \mathbf{k}_{\beta}\right)\cdot\left(\mathbf{r}_{A} - \mathbf{r}_{B}\right) \tag{22}$$

$$= M\sum_{i}\frac{q(k_{\alpha i} - k_{\beta i})E_{i}}{m}\left(\frac{1}{{\omega_{Ai}}^{2}} - \frac{1}{{\omega_{Bi}}^{2}}\right), \tag{23}$$

where, in the second line, equation (2) is used. $\phi^{A}_{\mathrm{PD}} - \phi^{B}_{\mathrm{PD}}$ reveals the difference between the ion equilibrium positions $\mathbf{r}_{AB}$ along the direction $\mathbf{k}_{\alpha} - \mathbf{k}_{\beta}$. Thus, $\phi^{A}_{\mathrm{PD}} - \phi^{B}_{\mathrm{PD}}$ is sensitive to $\mathbf{E}$ along the direction $\mathbf{d}$ which has components

$$d_{i} = (k_{\alpha i} - k_{\beta i})\left(\frac{1}{{\omega_{Ai}}^{2}} - \frac{1}{{\omega_{Bi}}^{2}}\right). \tag{24}$$

We demonstrated this method in our system, the results are shown in figure 6. The two laser beams are derived from the same source, they are each passed through a separate acousto-optic modulator (allowing each beam to be separately switched on and off, and allowing controlled phase shifts $\{\theta_{j}\}$ to be introduced), then each beam is guided through an optical fiber before it is focussed onto the ion. The path length difference from the point where the beams are separated to the experimental chamber, varies in time, due to temperature fluctuations and mechanical vibrations. Because of this $\left(\Phi_{\alpha 0} - \Phi_{\beta 0}\right)$ and thus ϕ^{A}_{PD} and ϕ^{B}_{PD} vary in time. We measured the drift of ϕ^{A}_{PD} and ϕ^{B}_{PD} in time using the sequence of figure 5 with $M = 1$ by interleaving measurements using trap settings A and B, and control phases $\theta_{\mathrm{T}} = 0$ and $-\frac{\pi}{2}$, and using equation (8). The results are shown in figure 6(a).

Because ϕ^{A}_{PD} and ϕ^{B}_{PD} do not drift too fast, and because the difference between the ion equilibrium positions $\mathbf{r}_{AB}$ is stable, the difference between the estimates $\phi^{A}_{\mathrm{PD}} - \phi^{B}_{\mathrm{PD}}$ is stable in time, as shown in figure 6(a).

We varied the voltage applied to a compensation electrode and measured the linear response of $\phi^{A}_{\mathrm{PD}} - \phi^{B}_{\mathrm{PD}}$, this is shown in figure 6(b). This result is consistent with equation (23), which describes a linear relationship between $\phi^{A}_{\mathrm{PD}} - \phi^{B}_{\mathrm{PD}}$ and a component of $\mathbf{E}$. Thus, the quantity $\phi^{A}_{\mathrm{PD}} - \phi^{B}_{\mathrm{PD}}$ can be used for minimizing micromotion.

Longer pulse sequences (with larger M) offer more precise measurement of $\phi^{A}_{\mathrm{PD}} - \phi^{B}_{\mathrm{PD}}$, though they also require better interferometric stability between the two beams. We expect the interferometric stability in our system is limited by fiber noise, which can be diminished using fiber noise cancellation [31].

3. Fast and accurate micromotion minimization

Using method A with $M = 8$ we minimized the strength of the offset field $\mathbf{E}$ quickly and accurately. This is shown by the data in figure 7. The experiment runs alternated between using two different laser beams from two different directions; in this way we probed $\mathbf{E}$ in two dimensions, i.e. the plane of the oscillating field of a linear Paul trap. We see that with increasing measurement time t the residual electric field strength decreased as $t^{-1/2}$, until around 100 s when drifts kicked in. The drifts were likely caused by changes in the offset field $\mathbf{E}$ and instability of the voltage sources used to apply voltages to the compensation electrodes.

We obtained the data as follows: first we measured the rate of change of ϕ_{PD} with respect to compensation electrode voltage, in much the same way as shown in figure 3(b). We did this for ϕ_{PD} measurements using the two different laser beams and two different compensation electrodes. Then we repetitively measured ϕ_{PD} using the two different laser beams, and every 11 s we updated the voltages of the two compensation electrodes so as to minimize $|\mathbf{E}|$ in two dimensions. We measured repetitively over 18 minutes. By analysing data collected over this time, we see how well the magnitude of the electric field $\mathbf{E}$ can be minimised with different measurement times. The analysis is much the same as that used to calculate the overlapping Allan deviation of fractional frequency data from a clock.

After 75 s of measurement the 2D residual static field strength was (3.5 ± 0.3) mV m^{-1}, which is, as far as we are aware, lower than the residual static field strength achieved using any other micromotion minimization technique, and also lower than the residual field achieved in a system of optically-trapped ions [32]. The field uncertainty decreased with increasing measurement time as (31.1 ± 1.0) mV m^{-1} s$^{1/2}$.

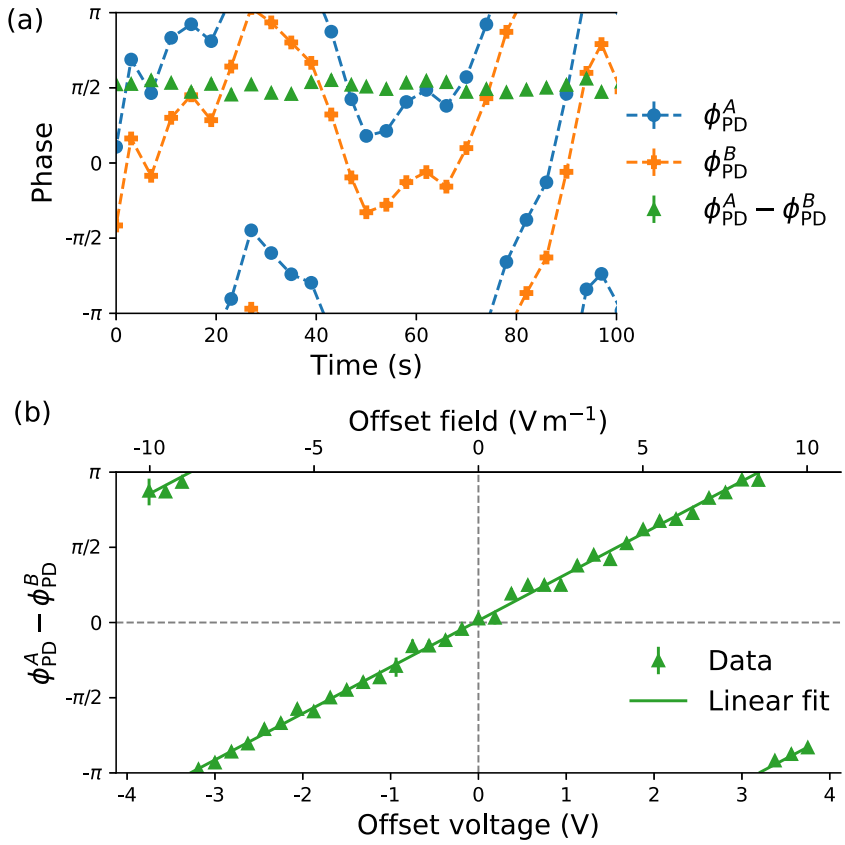

Figure 6. Demonstration of method B. (a) $\phi^A_{\rm PD}$ and $\phi^B_{\rm PD}$ were repeatedly measured over 100 s. The phase difference $\phi^A_{\rm PD} - \phi^B_{\rm PD}$ is stable in time, despite the drift of $\phi^A_{\rm PD}$ and the drift of $\phi^B_{\rm PD}$. (b) $\phi^A_{\rm PD} - \phi^B_{\rm PD}$ has a linear dependence on the offset voltage applied to a micromotion compensation electrode. Error bars representing quantum projection noise (1σ confidence interval) are generally smaller than the marker size.

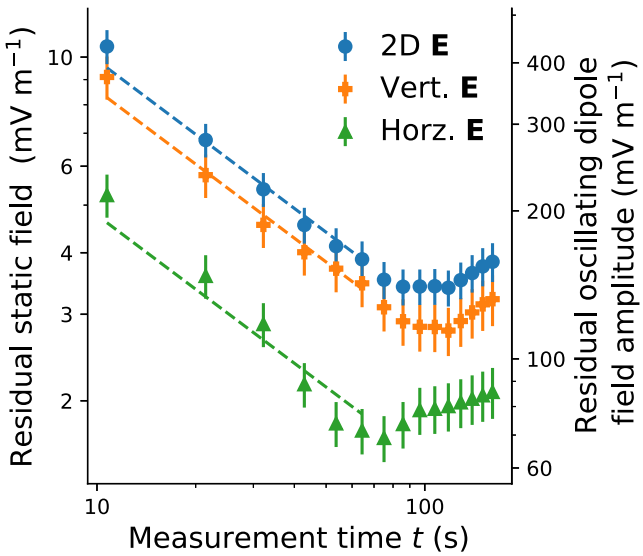

Figure 7. Using method A we minimized the magnitude of the offset field **E** quickly and accurately. With increasing measurement time t the residual field strength decreased as $t^{-1/2}$, until around 100 s when drifts caused the accuracy to worsen. Dashed lines are $t^{-1/2}$ fits. Error bars represent the standard error of the mean (1σ confidence interval).

The horizontal component of **E** was minimised faster than the vertical component, since the beam probing the horizontal component has a larger projection onto the plane of the oscillating field than the beam probing the vertical component.

On the second y-axis of figure 7 we show the corresponding strength of the residual oscillating dipole field experienced by the ion, which arises because the offset field **E** displaces the ion from the oscillating

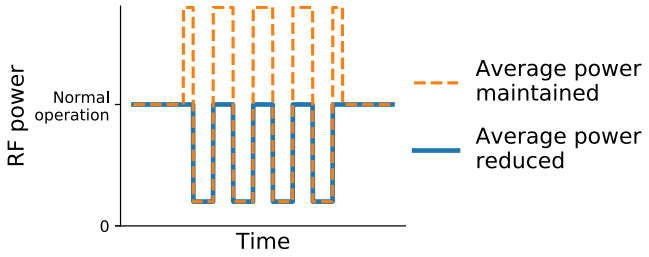

Figure 8. To mitigate unwanted changes of the trap temperature, the average RF power used during the interferometry sequences should equal the RF power used during normal trap operation. The RF power profiles sketched here are suitable for use with method A and $M = 8$.

quadrupole field null. This assumes that there is no additional oscillating dipole field in our system which arises from a phase mismatch of the voltages applied to the trap electrodes (quadrature micromotion) [1]. It is worth noting that a horizontal (vertical) offset field **E** causes the ion to experience a vertical (horizontal) oscillating dipole field (see figure 15).

The experiments were evenly split between using two different laser beams and four different sets of control phases $\{\theta_j\}$. The use of four sets of controllable phases diminished systematic errors, as is described in section 5. During these measurements we reduced the ion's radial secular frequencies from $2\pi \times 1.5$ MHz to $2\pi \times 840$ kHz, while keeping the axial secular frequency at $2\pi \times 350$ kHz. The oscillating quadrupole field's frequency was $2\pi \times 18.1$ MHz.

Faster minimization of **E** could be achieved using a larger change of the trap stiffness or by using a longer sequence (with higher M). A phase estimation sequence with over 1000 pulses has been conducted in an experimental setup with a longer coherence time than ours [33]. With such long sequences care must be taken to mitigate heating of the ion's motion caused by the trap stiffness changes. Ion heating causes pulse area errors, which in turn can cause systematic errors in ϕ_{PD} estimates. This can be mitigated by changing the trap stiffness sufficiently slowly, or by employing sympathetic cooling [9, 34]. Alternatively **E** can be probed using method B, which does not involve changes of the trap stiffness between the pulses.

3.1. Changing the RF power applied to the trap electrodes affects the trap temperature

After just 11 s measurement time we achieve a low residual oscillating dipole field, which would cause a second-order Doppler shift on the $^{88}Sr^{+}$ clock transition below the 10^{-22} level [1, 2]. And so, the micromotion minimization methods presented here stand to benefit precision spectroscopy experiments. However, in precision spectroscopy experiments, care should be taken to mitigate unwanted changes of the trap temperature.

Changing the trap stiffness by changing the RF power supplied to the trap electrodes affects the RF power dissipated in the system, which, in turn, affects the trap temperature. Changes of the trap temperature affect the blackbody radiation field experienced by the ion. Further, thermal expansion can shift the relative positions of trap electrodes and affect **E** [13], and also cause beam-pointing errors. During the measurements used to produce the data shown in figure 7 we did not make efforts to mitigate trap temperature changes. During these measurements the RF signal applied to the trap electrodes was reduced 4% of the time. We estimate that the decrease of the average RF power caused the temperature of the ion's surroundings to decrease by $\sim$10 mK [35], causing a blackbody radiation shift on the $^{88}Sr^{+}$ clock transition $\sim 10^{-19}$ [36].

To mitigate trap temperature changes the average RF power used during the micromotion minimization sequences should equal the RF power used during the trap's normal operation [13], for instance as sketched in figure 8. Alternatively, the trap stiffness can be changed during the micromotion minimization sequences by changing the amplitude of the trap's static quadrupole field [12, 13]. This relies on a perfect overlap between the nulls of the trap's oscillating and the static quadrupole fields, however, design errors and machining imprecision will cause the nulls to be separated.

4. Micromotion minimization with sub-standard quantum limit scaling using a binary search algorithm

In this section we use a binary search algorithm (based on the *robust phase estimation* technique [28]) to efficiently measure ϕ_{PD} of method A with an uncertainty below the standard quantum limit (SQL). The same methodology can be used together with methods B or C (supplemental material [29]). This phase

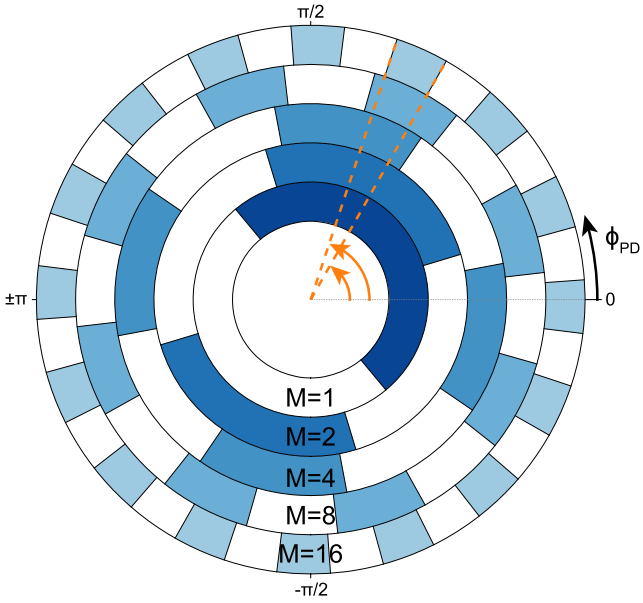

Figure 9. Illustration of the binary search algorithm (based on the *robust phase estimation* technique [28]). By conducting measurements using different sequence lengths $\phi_{\rm PD}$ can be determined efficiently. The shaded regions of width π/M indicate values of $\phi_{\rm PD}$ consistent with the measurement results. Shorter sequences allow $\phi_{\rm PD}$ to be reckoned from within a larger range, but they are less precise. Longer sequences are more precise, but they allow $\phi_{\rm PD}$ to be reckoned from within only a narrow range. By combining the results $\phi_{\rm PD}$ can be determined with high precision from a broad range. The orange arrows indicate the range of $\phi_{\rm PD}$ values consistent with all the measurement results.

estimation technique can be used to achieve Heisenberg scaling, it is easy to implement, the data analysis is straightforward and the protocol is non-adaptive. While adaptive phase estimation techniques allow for more accurate phase measurements at the Heisenberg limit [37, 38], they require measurement settings to be updated on the fly, which is not possible with our current control system [39–41].

The binary search algorithm works as follows: starting with an unknown phase $\phi_{\rm PD}$ from within the range $[-\pi, \pi]$, a set of measurements are first conducted using a sequence with $M = 1$ to limit $\phi_{\rm PD}$ to a range of width π, then a set of measurements with $M = 2$ narrow the range to $\pi/2$, then a set of measurements with $M = 4$ narrow the range to $\pi/4$, and so on. The jth set of measurements use a sequence with $M_j = 2^{j-1}$ to narrow the range to a width of $\pi/2^{j-1}$. The technique is illustrated in figure 9.

We demonstrated the efficiency of this protocol as follows: we carried out 59 000 measurement runs, split evenly between five sequence lengths $M \in \{1, 2, 4, 8, 16\}$. The measurements were also split between using two different $\theta_{\rm T}$ values. We then analysed the estimates of $\phi_{\rm PD}$ given by sub-sampled datasets. If we consider first the results using only $M = 1$ data, the error in the estimates of $\phi_{\rm PD}$ decreased with the number of measurements in the sample N as $N^{-1/2}$. This is shown by the data marked by blue circles in figure 10(a). The binary search algorithm allows improved estimates to be achieved using fewer measurements, as shown by the data marked by orange crosses. The first orange cross datapoint describes the error in estimates of $\phi_{\rm PD}$ using 40 measurements split evenly between different sequence lengths $M \in \{1, 2\}$. The second cross datapoint describes the error in estimates using 60 measurements split evenly between sequence lengths $M \in \{1, 2, 4\}$. And so on for the third and fourth cross datapoints. The scaling of the data marked by orange crosses with the number of measurements is well described by a power law. The deviation from the power law for the final datapoint (using sequences with up to $M = 16$) is due to the limited coherence time of our experiment and also because of the non-zero probability of error in the results of the measurements with $M < 16$, which contribute to the overall estimate. The 'true' value of $\phi_{\rm PD}$ was estimated using all 59 000 measurements.

The duration of each experimental run was dominated by cooling and fluorescence detection, rather than the duration of the coherent pulses. Thus, the x-axis in figure 10(a) reflects the total measurement time. For long sequences with large M the total measurement time would be better represented by the total area of coherent pulses $\mathcal{A}$ than by the number of measurements [42]. And so we rescale the x-axis of figure 10(a) to view the scaling of the same data with the pulse area, this is shown in figure 10(b). Here we see that the binary search algorithm allows us to estimate $\phi_{\rm PD}$ with an error below the SQL $\sqrt{\frac{\pi}{\mathcal{A}}}$ [43]. A better scaling would be achieved in an experimental setup with a longer coherence time. Also, to achieve Heisenberg scaling the different measurement sets (parameterised by j) need to use different numbers of measurements N_j [28].

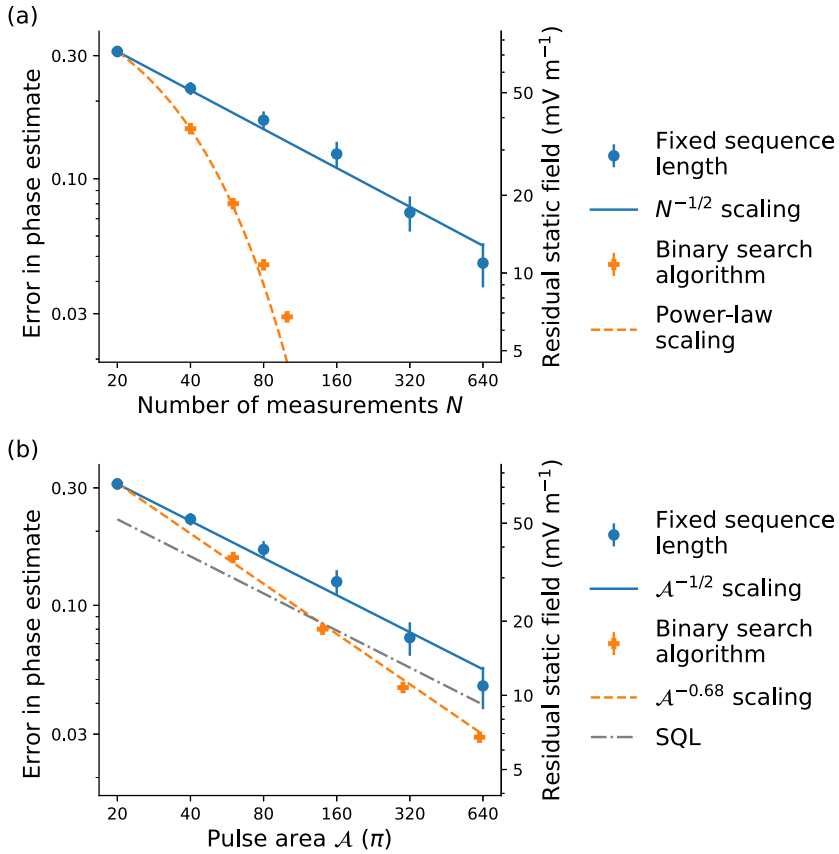

Figure 10. ϕ_{PD} can be efficiently measured using a binary search algorithm. Combining the results of measurements using different sequence lengths (data marked by orange crosses) is more efficient than using a fixed sequence length (data marked by blue circles). This is true both when the number of measurements conducted is considered, as in (a), and when the total pulse area is considered, as in (b). Using the binary search algorithm a ϕ_{PD}-uncertainty lower than the standard quantum limit (SQL) is achieved. Error bars represent the standard error of the mean (1σ confidence interval). The secondary y-axes show the uncertainty in the strength of the offset field $\mathbf{E}$ along one direction.

For readers interested in using the binary search algorithm in their systems we reproduce an algorithm for combining the results of different measurement sets from [33] in the supplemental material [29].

5. Robust estimates of ϕ_{T} using suitable control phases $\{\theta_j\}$

Changing the overall control phases θ_{T} (equation (6)) shifts the dependence of p on ϕ_{T}, as can be appreciated from equation (4) and figure 3(a). By appropriately choosing the individual phases θ_j, estimates of ϕ_{T} can be made robust against laser detuning and pulse area errors. Pulse area errors can arise if the sequence includes fast changes of the trap stiffness, which can cause motional heating, which in turn modifies the $|g\rangle \leftrightarrow |e\rangle$ coupling strength. They can also be caused by the change in laser light intensity when the ion changes position within a tightly-focussed laser beam.

We used simulations to test different sets of control phases $\{\theta_j\}$ when the pulse sequences from methods A and B are used, and we found control phase settings which allow ϕ_{T} (and thus ϕ_{PD}, ϕ^A_{PD} and ϕ^B_{PD}) to be robustly estimated in the presence of these errors when ϕ_{T} is small. We refer to the control phase settings as settings I: $\{\theta_{\mathrm{e}} = 0, \theta_{\mathrm{o}} = -\frac{\pi}{2}\}$ and settings II: $\{\theta_{\mathrm{e}} = 0, \theta_{\mathrm{o}} = \frac{\pi}{2}\}$, where

$$\theta_j = \begin{cases} \theta_{\mathrm{e}} & \text{even } j \\ \theta_{\mathrm{o}} & \text{odd } j, 1 < j < M+1 \end{cases} \tag{25}$$

as shown in figure 11. Both settings use $\theta_1 \in \{\pi, \frac{\pi}{2}\}$, $\theta_{M+1} = \pi$ and even values of M. Using these settings ϕ_{T} can be estimated using

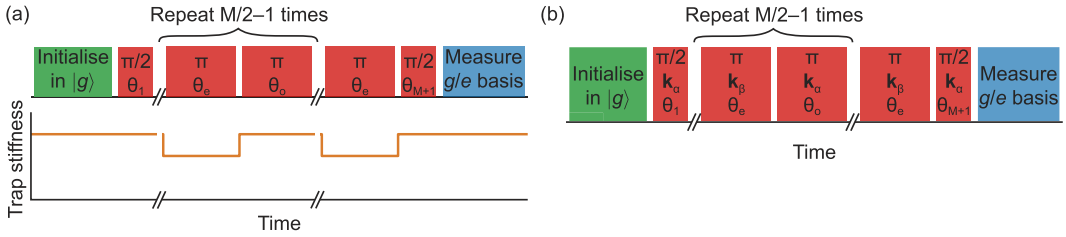

Figure 11. Pulse sequences showing control phases θ_e and θ_o used in control phase $\{\theta_j\}$ settings I, II and III. (a) and (b) Show the sequences used for methods A and B respectively.

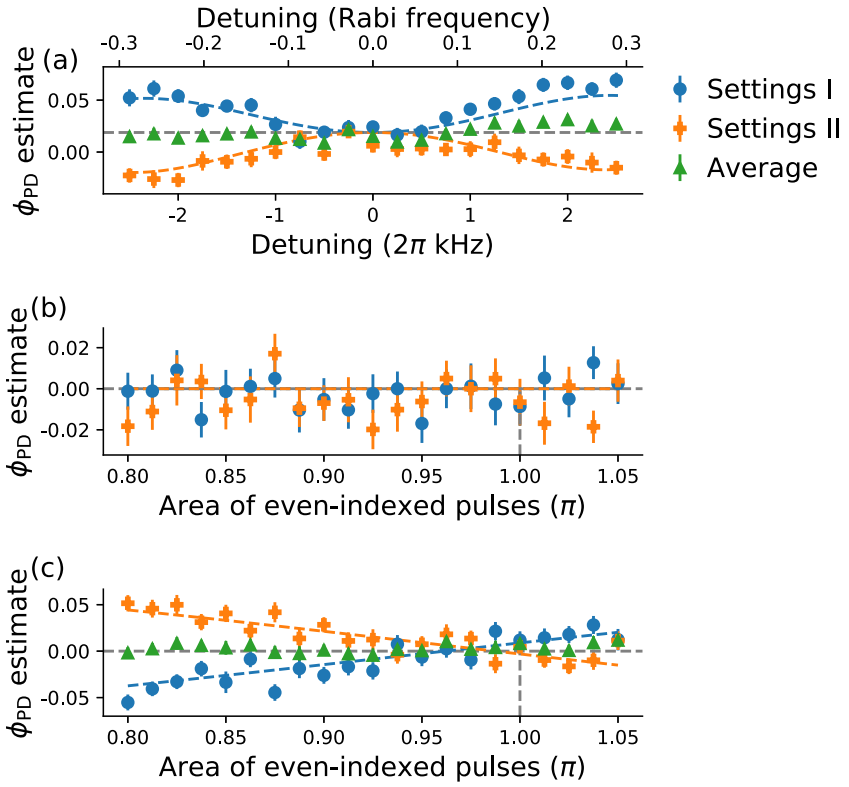

Figure 12. Estimates of ϕ_{PD} (and ϕ^A_{PD} and ϕ^B_{PD}) are robust against errors when the control phase $\{\theta_j\}$ settings I and II are used. The robustness is improved by averaging the estimates obtained using settings I and II. (a) The detuning of the laser from the $|g\rangle \leftrightarrow |e\rangle$ resonance was scanned. (b) and (c) A pulse area error on even-indexed pulses was introduced and varied, in (b) no additional errors were added, in (c) a 10% error was introduced to the area of odd-indexed pulses. Dashed lines indicate simulation results, which show good agreement with the experimental results; the only free parameter was a phase offset used in (a) which accounts for a weak offset field **E**. Error bars represent quantum projection noise (1σ confidence interval). The results in (b) and (c) were obtained using sequences with a fixed trap stiffness and a fixed laser field wavevector.

$$\phi_T = \arctan 2 \left\{ (-1)^{M/2} \left[p\left(\theta_1 = \frac{\pi}{2}\right) - \frac{1}{2} \right], \right. \tag{26}$$

$$\left. (-1)^{M/2} \left[p\left(\theta_1 = \pi\right) - \frac{1}{2} \right] \right\} \tag{27}$$

We experimentally tested the robustness of ϕ_{PD} estimates by introducing different errors to our system. The results are shown in figure 12.

First we measured ϕ_{PD} of method A with $M = 16$, when different laser detunings were used. One might expect that a detuning Δ might shift ϕ_T by $\Delta \cdot T$ and ϕ_{PD} by $\Delta \cdot T/M$, where the duration of the coherent pulse sequence T we used was 1.6 ms. The ϕ_{PD} estimates using settings I and II were much more stable than this, as shown in figure 12(a). Furthermore, the estimate of ϕ_{PD} becomes still more stable by averaging the estimates obtained with settings I and II.

Then we investigated the robustness in the presence of pulse area errors. We conducted experiments with a pulse area error on the even-indexed pulses. The phase estimates were stable when the magnitude of

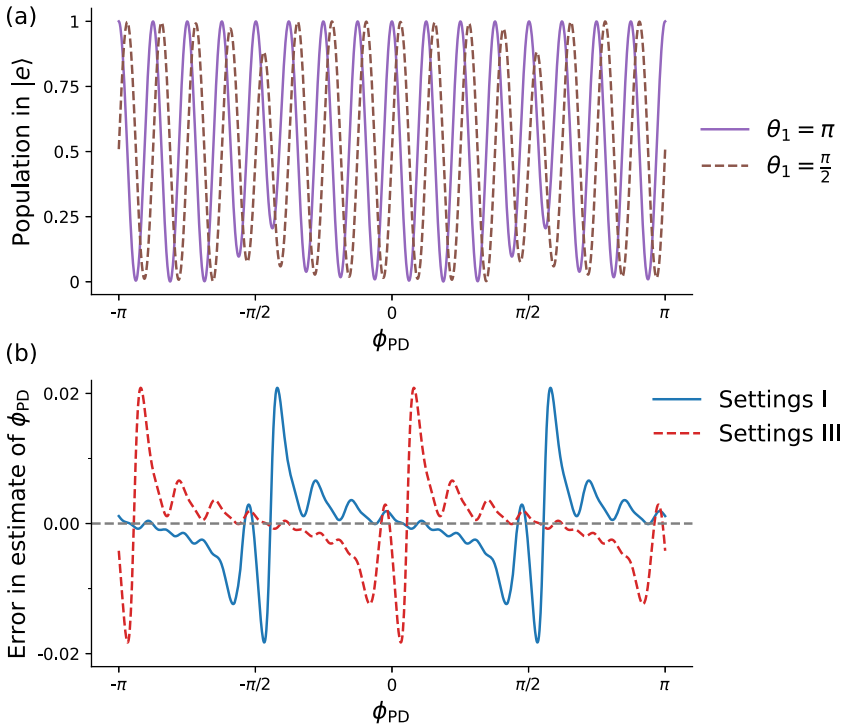

Figure 13. Pulse area errors and laser detuning cause systematic errors in estimates of ϕ_{PD}, the size of the errors depend on the control phases $\{\theta_j\}$ used and the true value of ϕ_{PD}. We show this using simulated experimental runs using sequences with $M = 16$ in which the even-indexed pulses have a 5% pulse area error. (a) Control phase settings I were used and the pulse area error affected the probability p of measuring the ion in state $|e\rangle$ most strongly around $\phi_{PD} = \pm\frac{\pi}{2}$ where the oscillation contrast was reduced. (b) Estimates of ϕ_{PD} were generated from the simulated runs. With control phase settings I the accuracy is highest near $\phi_{PD} = 0$ or π, while with settings III the accuracy is highest near $\phi_{PD} = \pm\pi/2$.

this error was varied, as shown in figure 12(b). We additionally introduced a 10% pulse area error on the odd-indexed pulses, and found that the robustness of the phase estimate could again be improved by averaging the results of experiments conducted using settings I and II, as shown in figure 12(c). These experiments used $M = 8$, a fixed trap stiffness and a single laser beam driving the pulses. The reason we alternated the pulse area error between pulses is that this will happen in practice, since in method A the trap stiffness setting is alternated, while in method B the laser beam is alternated.

The robustness properties depend on the size of the phase ϕ_{PD}, as shown by the simulation results in figure 13. We simulated experimental runs using pulse sequences of length $M = 16$ with pulse area errors of 5% on the even-indexed pulses. The results of simulations using control phase settings I are shown in figure 13(a); we see that the probability p of measuring the ion in state $|e\rangle$ deviates from the unity-contrast oscillations described by equation (14), at around $\phi_{PD} = \pm\frac{\pi}{2}$. From this data estimates of ϕ_{PD} were generated, and the systematic errors in the estimates (caused by the 5% pulse area error) were largest when the true value of ϕ_{PD} was around $\pm\frac{\pi}{2}$, as shown in figure 13(b). We also simulated measurements using control phase settings III (described in the Supplemental Material [29]), then the systematic errors in ϕ_{PD} estimates were largest when the true value of ϕ_{PD} was near 0 or π.

Although the robustness of phase estimates depends on the true value of the phase, this is unlikely to be a problem when method A is used and when micromotion is nearly minimized—then ϕ_{PD} is small and control phase settings I and II perform well. However, if method B is used in an experiment setup in which the path length difference between the two laser beams is not stable, then ϕ^A_{PD} and ϕ^B_{PD} will drift over time (as shown in figure 6(a)) and the robustness of the phase estimates will be unstable. This instability could be mitigated by adapting the control phase values during a measurement on the fly, for instance, if the first few measurement runs indicate $\phi^A_{PD} \approx 0$ or π ($\frac{\pi}{2}$ or $-\frac{\pi}{2}$) then the control phase settings could be switched to settings I (settings III), which perform robustly around these phase values, as shown in figure 13.

To gain an intuition of why the pulse sequences are robust against errors, we show the evolution of the ion state during a sequence in the supplemental material [29].

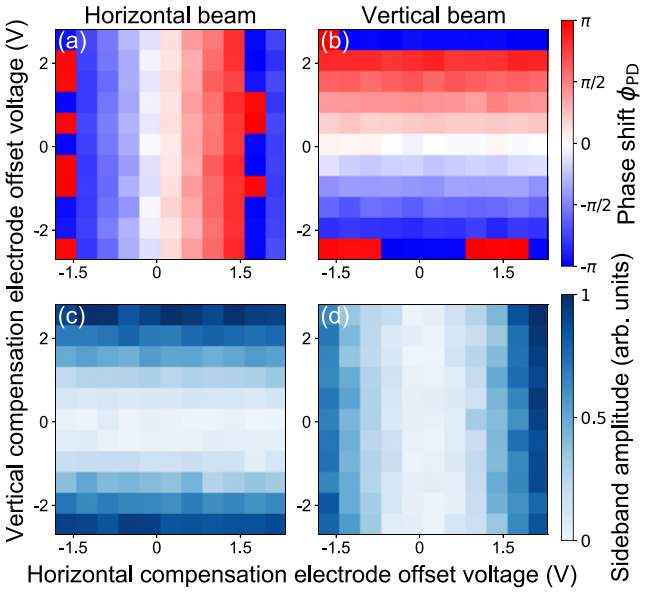

Figure 14. |**E**| can be minimized in 2D using a single probe laser, by using interferometry method A together with the resolved sideband technique [1]. (a) and (b) ((c) and (d)) Use the interferometry (resolved sideband) method, (a) and (c) ((b) and (d)) use a horizontal (vertical) probe beam.

6. Micromotion minimization in 2D and 3D

6.1. Applying the interferometry methods in 2D and 3D

To counter an unwanted electric field **E** in 2D (3D) we produce a 2D (3D) compensating field by supplying voltages to two (three) compensation electrodes. To determine the appropriate voltages we need to measure ϕ_{PD} or $\phi^{A}_{\mathrm{PD}} - \phi^{B}_{\mathrm{PD}}$ using two (three) laser beam configurations. First we measure the dependence of the ith phase measurement on the jth compensation electrode voltage, in the same way as in figure 3(b) or figure 6(b). We label the gradient of this dependence $\mathcal{M}_{ij}$. We use the four (nine) $\mathcal{M}_{ij}$ values to construct a 2×2 (3×3) matrix $\mathcal{M}$. Then we can minimize |**E**| by measuring the two (three) phase values, storing them in a two-element (three-element) vector $\boldsymbol{\phi}$, then calculating $\mathbf{V} = \mathcal{M}^{-1} \cdot \boldsymbol{\phi}$ [44]. The two-element (three-element) vector **V** describes the offsets of the compensation electrode voltages from the optimal values. Note that the matrix $\mathcal{M}$ depends on the trap settings used.

If one wishes to relate $\boldsymbol{\phi}$ to the offset field **E**, one can use equation (12) or equation (23). This requires knowledge of the direction of the laser field wavevectors and the change of the secular frequencies. Alternatively one can relate **V** to **E** using another micromotion minimization technique; in this work we related **V** to **E** using the resolved sideband method [1, 2].

6.2. 2D micromotion minimization using a single probe laser beam

Micromotion can be minimized in two dimensions using a single probe laser beam by using the resolved sideband method [1] together with interferometry method A. This is shown in figure 14. In figure 14(a) the interferometry method is conducted using a horizontal laser beam, and ϕ_{PD} is sensitive to the horizontal component of **E**, which is varied by changing the voltage applied to the 'horizontal' compensation electrode. In figure 14(c) the resolved sideband method is conducted using the same horizontal laser beam, and the sideband amplitude is sensitive to the vertical component of **E**, which is varied by changing the voltage applied to the 'vertical' compensation electrode. Similar results are observed when using a vertical laser beam in figures 14(b) and (d).

These results can be understood with the aid of figure 15. Using a horizontal laser beam and interferometry method A, the results are sensitive to the horizontal component of **E**, which displaces the ion equilibrium position horizontally. Using a horizontal laser beam and the resolved sideband method, the results are sensitive to the vertical component of **E**, which displaces the ion equilibrium position vertically, at the new equilibrium position the ion experiences a horizontal oscillating dipole field, which drives horizontal micromotion.

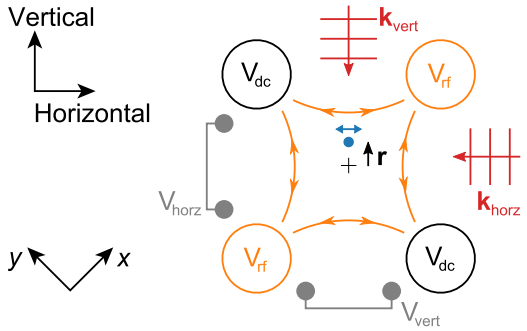

Figure 15. Schematic of the experimental setup, showing a slice through the linear Paul trap in the plane of the oscillating electric field. The trap's oscillating electric quadrupole field (orange lines) is produced by applying voltages to four electrodes (large circles). An unwanted dipolar field along the vertical direction displaces the ion equilibrium position vertically, with displacement **r** from the trap centre (black cross). This can be detected using interferometry method A with the vertical laser beam, or using the resolved sideband method with the horizontal laser beam, since at the new position the ion (blue dot) experiences a horizontal oscillating dipole field which drives horizontal micromotion (blue arrow). Each compensation electrode consists of a pair of rods (grey circles). The ion's secular motion eigenmodes are orientated along x and y.

6.3. Applying the interferometry methods in linear Paul traps with non-degenerate radial frequencies

Micromotion minimization techniques that involve monitoring an ion's position when the trap stiffness is changed become more sensitive when larger changes of the trap stiffness are used. However, in a linear Paul trap, if the trap stiffness is reduced to the point where the ion is barely trapped, and if non-degenerate radial secular frequencies are used, these techniques risk becoming overwhelmingly sensitive to the offset field **E** along just one direction.

We illustrate this behaviour in figure 16. The calculations show how the trap stiffnesses respond when the amplitude of the linear Paul trap's oscillating quadrupole field is changed, from an initial setting A, with non-degenerate trap stiffnesses $\{\omega_{Ax}, \omega_{Ay}\}/2\pi = \{1.5, 1.6\}$ MHz along the radial directions and $\omega_{Az}/2\pi = 1.0$ MHz along the axial direction, to a trap setting B. As we decrease the amplitude of the trap's oscillating quadrupole field $\omega_{Bx} \to 0$ before $\omega_{By} \to 0$ and thus the quantity $\omega_{Bx}^{-2} - \omega_{Ax}^{-2}$ diverges before $\omega_{By}^{-2} - \omega_{Ay}^{-2}$ diverges. These quantities describes the response of $\mathbf{r}_{AB}$ to **E** (equation (2)) and impact the direction **d** along which the interferometry method is sensitive to **E** (equations (13) and (24)). As a result, when method A is used with a beam that has a projection onto both the x and y axes, and when the oscillating quadrupole field amplitude is reduced to the point where the ion is barely trapped ($\omega_{Bx} \approx 0$) the technique effectively becomes sensitive to only E_x. A much higher sensitivity to E_x than to E_y also appears if the radial stiffnesses are reduced by increasing the amplitude of the static quadrupole field which provides axial confinement.

We illustrate this sensitivity difference by conducting experiments using method A as E_x and E_y are changed, using two different laser beams which each have projections onto the x and y axes. The beam directions are shown in the schematic in figure 15. The results are shown in figure 17. In figures 17(a) and (b) the secular frequencies are degenerate ($\omega_x = \omega_y$), and ϕ_{PD} depends on the vertical (horizontal) component of **E** when a vertical (horizontal) probe beam is used; the orthogonal beams are sensitive to orthogonal components of **E**. In figures 17(c) and (d) the secular frequencies are non-degenerate with $\omega_x < \omega_y$ and the method becomes more sensitive to E_x than to E_y. As a result, the orthogonal beams are sensitive to non-orthogonal components of **E**.

If a higher sensitivity to E_x than to E_y is problematic, method C (supplemental material [29]) may be useful; it allows the direction of sensitivity **d** to be tuned. Another solution is to implement method A using a probe beam propagating along the y-axis, with no projection onto the x-axis. However, in most setups the electrode geometry obstructs optical access along the directions of secular motion. A third solution is to calculate superpositions of the phases measured via method A using probe beams from different directions, for instance a weighted sum (difference) of the phases measured with the horizontal and vertical beams is sensitive to $E_x(E_y)$. Alternatively one can use method B, with two beams whose wavevector difference $\mathbf{k}_\alpha - \mathbf{k}_\beta$ has no x-component (see equation (24)).

6.4. Minimization of axial micromotion in a linear Paul trap

In an ideal linear Paul trap there is no RF electric field along the trap symmetry axis (z direction) $\tilde{E}_z = 0$. In physical linear Paul traps, $\tilde{E}_z$ is non-zero because of the finite size of the trap electrodes, among other reasons [2, 45–47]. A non-zero $\tilde{E}_z$ drives ion micromotion along z. Usually $\tilde{E}_z$ vanishes only at a single point, and with increasing distance from this point along z, $|\tilde{E}_z|$ increases [46] and the extent of axial

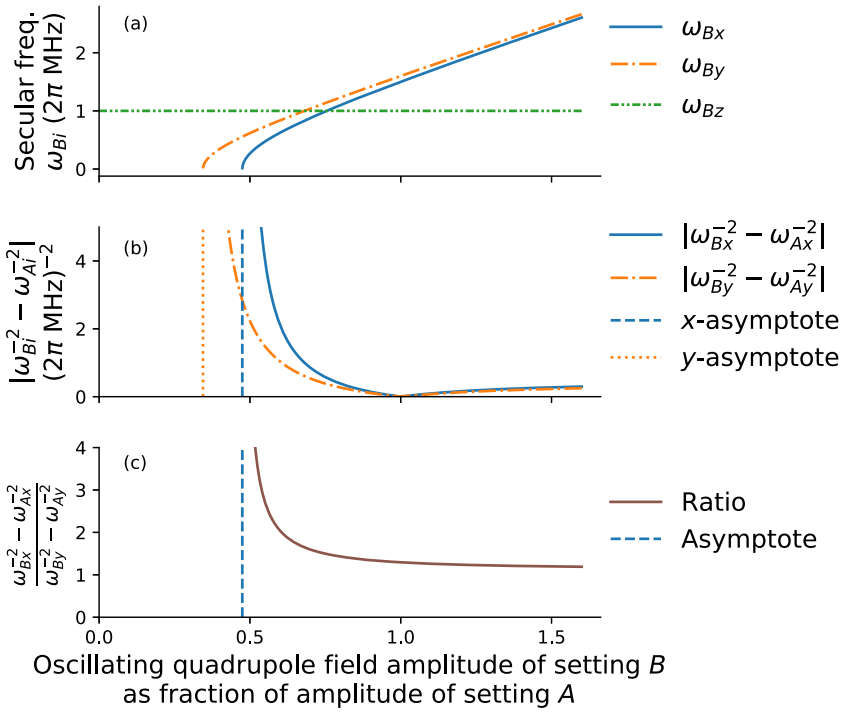

Figure 16. When the radial trapping frequencies in a linear Paul trap are non-degenerate with $\omega_x < \omega_y$, an offset field along the x-direction causes a larger change of ion equilibrium position than an offset field of the same magnitude along the y-direction. This difference diverges as the amplitude of the oscillating quadrupole field is reduced. In the figure the trap stiffness is changed between initial settings A with $\{\omega_x, \omega_y, \omega_z\}/2\pi = \{1.5, 1.6, 1.0\}$ MHz and settings B by changing the amplitude of the oscillating quadrupole field. (a) As the oscillating quadrupole field amplitude during setting B is decreased, $\omega_{Bx} \to 0$ before $\omega_{By} \to 0$. (b) The ion displacement r_{ABi} due to an offset field E_i depends on $\omega_{Bi}^{-2} - \omega_{Ai}^{-2}$ (see equation (2)). This quantity diverges as $\omega_{Bi} \to 0$. (c) The ratio of $\omega_{Bx}^{-2} - \omega_{Ax}^{-2}$ to $\omega_{By}^{-2} - \omega_{Ay}^{-2}$, indicating the relative displacements caused by an offset field, diverges as the trap stiffness during setting B is reduced and $\omega_{Bx} \to 0$.

micromotion increases. Thus, the null point can be found using, for example, the resolved sideband method [1] with a laser beam propagating along the z direction.

Because the extent of axial micromotion and thus the kinetic energy associated with it increase with distance along z from the null, $\tilde{E}_z$ introduces a trapping pseudopotential along z. This pseudopotential contributes to the axial confinement, and this means that axial micromotion can be minimised using methods which are sensitive to the change of ion equilibrium position along z when ω_z is changed [13]. And so, we demonstrated that interferometry method A can be used to minimize axial micromotion:

We varied the z-component of $\mathbf{E}$ (and thus we varied $\tilde{E}_z$) by changing the voltage applied to an endcap electrode, and we measured the linear response of ϕ_{PD} using a laser beam with wavevector $\mathbf{k}$ largely along the z-direction (it propagates through holes in the endcap electrodes). We changed ω_z during the pulse sequence by changing the amplitude of the oscillating electric quadrupole field. The results are shown in figure 18. The zero-offset voltage was determined using the resolved sideband method [1]; the optimal voltage determined using the interferometry method and the optimal voltage determined using the resolved sideband method do not perfectly agree. This mismatch may have resulted from a small projection of the probing laser beam onto the x and y directions (the plane of the oscillating quadrupole field) together with non-zero x- and y-components of $\mathbf{E}$.

7. Demonstration of quantum clock synchronization protocols

Method A has much in common with two quantum clock synchronization protocols [25, 26]. Synchronizing distant clocks is important for engineering and metrology. It is also of fundamental interest in physics, falling within the field of reference frame alignment [48]. Suppose Alice and Bob want to synchronize their clocks, which are known to tick at the same rate: Eddington's protocol [49] involves Alice synchronizing a watch to her clock, and then mailing the watch to Bob, who synchronizes his own clock to the watch. Chuang [25] proposed a quantum version of Eddington's protocol, in which Alice sends a quantum watch to Bob, namely a ticking qubit. In this protocol Alice and Bob each apply a $\pi/2$ pulse on the qubit before the state of the qubit is measured. Importantly, the phase of each $\pi/2$ pulse is relative to Alice's and Bob's clocks respectively.

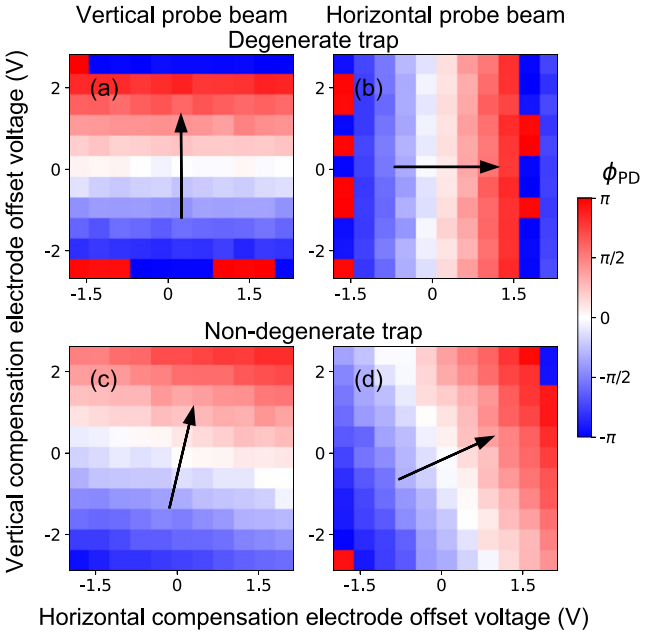

Figure 17. 2D micromotion compensation with degenerate secular frequencies compared with the case of non-degenerate secular frequencies. In (a) ((b)) the secular frequencies are degenerate, and ϕ_{PD} is sensitive to the vertical (horizontal) component of **E** along $\frac{1}{\sqrt{2}}(\hat{x}+\hat{y})$ ($\frac{1}{\sqrt{2}}(\hat{x}-\hat{y})$) when measured using a vertical (horizontal) beam. In (c) and (d) the secular frequencies are non-degenerate, with $\omega_x < \omega_y$, and as a result the measurements of ϕ_{PD} become more sensitive to **E** along the x-direction, i.e. the 'horizontal + vertical' direction, as described by equation (13) and figure 16.

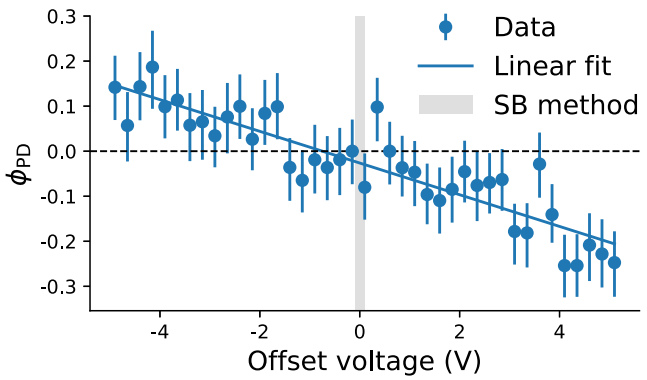

Figure 18. The interferometry sequences enable axial micromotion compensation in a linear Paul trap. The axial component of **E** is varied by offsetting the voltage applied to an endcap electrode, and ϕ_{PD} responds linearly. ϕ_{PD} is measured using method A with a beam propagating along the axial direction. Error bars represent quantum projection noise (1σ confidence interval). The shaded area indicates the 1σ uncertainty in the estimate obtained using the resolved sideband method.

The sequence of method A with $M = 1$ is equivalent to Chuang's protocol. In this sequence the trapped ion equilibrium position changes from $\mathbf{r}_A$ (Alice's location) to $\mathbf{r}_B$ (Bob's location) when the trap stiffness is changed. We identify the optical field at $\mathbf{r}_A$ as Alice's clock, and the optical field at $\mathbf{r}_B$ as Bob's clock (these clocks tick incredibly fast, at over 400 THz). The asynchronicity of the clocks is due to the phase difference ϕ_{PD} between the optical field at $\mathbf{r}_A$ and the optical field at $\mathbf{r}_B$ (see equation (11)). During the sequence we first apply a $\pi/2$ pulses on a ticking ion qubit at position $\mathbf{r}_A$ (the pulse phase is determined by Alice's clock) then we move the qubit to $\mathbf{r}_B$ and apply another $\pi/2$ pulse (the pulse phase is determined by Bob's clock), before measuring the state of the qubit. Measurements allow us to calculate ϕ_{PD} and thus 'synchronize the clocks', as shown in figure 3. In figure 19 we illustrate the relationship between method A and Chuang's protocol.

De Burgh and Bartlett [26] improved on Chuang's protocol. They proposed that Alice and Bob perform multiple exchanges of the qubit, and apply multiple pulses on the qubit, to more accurately determine ϕ_{PD}.

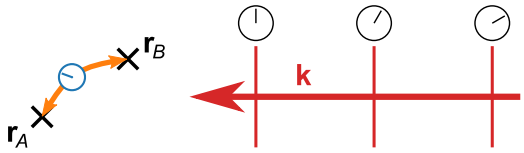

Figure 19. Method A is related to quantum versions of Eddington's clock synchronization protocol [25, 26]: Alice and Bob (phantoms at $\mathbf{r}_A$ and $\mathbf{r}_B$) have an unknown phase difference ϕ_{PD} between their clocks (the oscillating laser field at their positions). They exchange a ticking qubit (a trapped ion), and they each perform rotations on it. By measuring the difference between their rotation axes they learn ϕ_{PD}.

Method A with $M > 1$ is equivalent to this protocol, and the data in figures 4 and 10 demonstrates the enhancement gained from this protocol over the two-pulse protocol[6].

Within the framework developed in this section, we can describe method B as a protocol to synchronize two oscillators (i.e. two laser fields) which are at the same position, using a ticking qubit.

8. Conclusion

We introduce and demonstrate interferometry pulse sequences for minimizing the magnitude of a stray electric field $\mathbf{E}$ in a trapped ion experiment. These sequences allow $|\mathbf{E}|$ to be minimized to state-of-the-art levels quickly. These methods will be particularly useful in trapped ion precision spectroscopy experiments [2, 50], hybrids systems of neutral atoms and trapped ions [5–8], and experiments using highly-polarizable Rydberg ions [3, 4], which are very sensitive to effects caused by stray fields.

We demonstrate that quantum phase estimation techniques can be used to minimize $|\mathbf{E}|$ with a scaling below the standard quantum limit. This constitutes a real-world case in which quantum metrology provides a significant enhancement. We also show that the results can be robust against laser detuning and pulse area errors.

By using one of the sequences presented here together with the resolved sideband method we minimize $|\mathbf{E}|$ in 2D using a single probe beam. This approach will be useful in experiments with restricted optical access, such as cavity QED experiments [51–53] and surface trap experiments [54–59].

We reduced $|\mathbf{E}|$ beyond state-of-the-art levels quickly. $|\mathbf{E}|$ could be reduced much further and much more quickly in a setup with a longer coherence time (allowing longer sequences) and with finer control of the trap stiffness (allowing larger stiffness changes).

In trapped ion precision spectroscopy experiments usually just a single ion is probed. Scaling up precision spectroscopy experiments to many ions enables faster interrogation [46, 47, 60, 61]. In a many-ion system the offset field $\mathbf{E}$ would ideally be measured and countered for each of the ions. The methods presented here will work in a system of many ions, provided that the ions do not unexpectedly switch positions during the sequences. Further, by probing a system of entangled ions, it might be possible to precisely measure offset fields even faster [62].

The methods we introduce can also be used when the states which get excited are separated by a Raman transition or a multi-photon transition. To achieve the highest sensitivity the laser beams should be orientated to give the largest effective wavevector.

The dominant cause of excess micromotion is usually a slowly-varying dipole field $\mathbf{E}$ at the null of the oscillating quadrupole field. However, excess micromotion can also arise when the oscillating voltages applied to the trap electrodes are out of phase, this is called quadrature micromotion. Measurements sensitive to $\mathbf{r}_{AB}$, such as the techniques presented here, do not give information about quadrature micromotion. Quadrature micromotion can instead be characterised using other methods [1, 2] and it can be avoided by careful trap design and fabrication [45, 46, 63].

Finally, our work demonstrates quantum versions of Eddington's clock synchronization protocol [25, 26], linking trapped ion experiments to the problem of reference frame alignment [48].

[6] Chuang's paper [25] includes a protocol with a sub-SQL scaling, however, this protocol requires a set of ticking qubits, whose frequencies span an exponentially-large range.

Acknowledgments

We thank Holger Motzkau for designing and making the bias tee in figure S3 (supplemental material [29]). We thank Ferdinand Schmidt-Kaler for making us aware of reference [64]. This work was supported by the Knut & Alice Wallenberg Foundation (Photonic Quantum Information and through the Wallenberg Centre for Quantum Technology (WACQT)), the QuantERA ERA-NET Cofund in Quantum Technologies (ERyQSenS), and the Swedish Research Council (Trapped Rydberg Ion Quantum Simulator and Grant No. 2020-00 381).

Conflict of interest

The authors wish to inform readers that they are the inventors and patent owners of inventions which are discussed in methods A, B and C. The journal has considered this, and it believes the conflict of interest in this case does not unduly influence the submission process or impact the quality of the paper.

Data availability statement

The data that support the findings of this study are available upon reasonable request from the authors.

ORCID iDs

Gerard Higgins https://orcid.org/0000-0003-0946-8067
Markus Hennrich https://orcid.org/0000-0003-2955-7980

References

[1] Berkeland D J, Miller J D, Bergquist J C, Itano W M and Wineland D J 1998 Minimization of ion micromotion in a Paul trap *J. Appl. Phys.* **83** 5025–33
[2] Keller J, Partner H L, Burgermeister T and Mehlstäubler T E 2015 Precise determination of micromotion for trapped-ion optical clocks *J. Appl. Phys.* **118** 104501
[3] Higgins G, Pokorny F, Zhang C and Hennrich M 2019 Highly polarizable Rydberg ion in a Paul trap *Phys. Rev. Lett.* **123** 153602
[4] Feldker T, Bachor P, Stappel M, Kolbe D, Gerritsma R, Walz J and Schmidt-Kaler F 2015 Rydberg excitation of a single trapped ion *Phys. Rev. Lett.* **115** 173001
[5] Grier A T, Cetina M, Oručević F and Vuletić V 2009 Observation of cold collisions between trapped ions and trapped atoms *Phys. Rev. Lett.* **102** 223201
[6] Schmid S, Härter A and Denschlag J H 2010 Dynamics of a cold trapped ion in a Bose–Einstein condensate *Phys. Rev. Lett.* **105** 133202
[7] Zipkes C, Palzer S, Sias C and Köhl M 2010 A trapped single ion inside a Bose–Einstein condensate *Nature* **464** 388
[8] Feldker T, Fürst H, Hirzler H, Ewald N V, Mazzanti M, Wiater D, Tomza M and Gerritsma R 2020 Buffer gas cooling of a trapped ion to the quantum regime *Nat. Phys.* **16** 413–6
[9] Barrett M D *et al* 2003 Sympathetic cooling of $^{9}Be^{+}$ and $^{24}Mg^{+}$ for quantum logic *Phys. Rev.* A **68** 042302
[10] Allcock D T C *et al* 2010 Implementation of a symmetric surface-electrode ion trap with field compensation using a modulated Raman effect *New J. Phys.* **12** 053026
[11] Chuah B L, Lewty N C, Cazan R and Barrett M D 2013 Detection of ion micromotion in a linear Paul trap with a high finesse cavity *Opt. Express* **21** 10632–41
[12] Schneider T, Peik E and Tamm C 2005 Sub-hertz optical frequency comparisons between two trapped $^{171}Yb^{+}$ ions *Phys. Rev. Lett.* **94** 230801
[13] Gloger T F, Kaufmann P, Kaufmann D, Baig M T, Collath T, Johanning M and Wunderlich C 2015 Ion-trajectory analysis for micromotion minimization and the measurement of small forces *Phys. Rev.* A **92** 043421
[14] Brown K R, Clark R J, Labaziewicz J, Richerme P, Leibrandt D R and Chuang I L 2007 Loading and characterization of a printed-circuit-board atomic ion trap *Phys. Rev.* A **75** 015401
[15] Ibaraki Y, Tanaka U and Urabe S 2011 Detection of parametric resonance of trapped ions for micromotion compensation *Appl. Phys.* B **105** 219–23
[16] Narayanan S, Daniilidis N, Möller S A, Clark R, Ziesel F, Singer K, Schmidt-Kaler F and Häffner H 2011 Electric field compensation and sensing with a single ion in a planar trap *J. Appl. Phys.* **110** 114909
[17] Tanaka U, Masuda K, Akimoto Y, Koda K, Ibaraki Y and Urabe S 2012 Micromotion compensation in a surface electrode trap by parametric excitation of trapped ions *Appl. Phys.* B **107** 907–12
[18] Härter A, Krükow A, Brunner A and Hecker Denschlag J 2013 Minimization of ion micromotion using ultracold atomic probes *Appl. Phys. Lett.* **102** 221115
[19] Mohammadi A, Wolf J, Krükow A, Deiß M and Hecker Denschlag J 2019 Minimizing rf-induced excess micromotion of a trapped ion with the help of ultracold atoms *Appl. Phys.* B **125** 122
[20] Yu N, Zhao X, Dehmelt H and Nagourney W 1994 Stark shift of a single barium ion and potential application to zero-point confinement in a rf trap *Phys. Rev.* A **50** 2738–41
[21] Cerchiari G, Araneda G, Podhora L, Slodička L, Colombe Y and Blatt R 2021 Measuring ion oscillations at the quantum level with fluorescence light *Phys. Rev. Lett.* **127** 063603

[22] Zhukas L A, Millican M J, Svihra P, Nomerotski A and Blinov B B 2021 Direct observation of ion micromotion in a linear Paul trap *Phys. Rev.* A **103** 023105
[23] Nadlinger D P, Drmota P, Main D, Nichol B C, Araneda G, Srinivas R, Stephenson L J, Ballance C J and Lucas D M 2021 Micromotion minimisation by synchronous detection of parametrically excited motion arXiv:2107.00056
[24] Saito R, Saito K and Mukaiyama T 2021 Measurement of ion displacement via RF power variation for excess micromotion compensation *J. Appl. Phys.* **129** 124302
[25] Chuang I L 2000 Quantum algorithm for distributed clock synchronization *Phys. Rev. Lett.* **85** 2006–9
[26] de Burgh M and Bartlett S D 2005 Quantum methods for clock synchronization: beating the standard quantum limit without entanglement *Phys. Rev.* A **72** 042301
[27] Chwalla M 2009 Precision spectroscopy with $^{40}Ca^{+}$ ions in a Paul trap *PhD thesis* Universität Innsbruck
[28] Kimmel S, Low G H and Yoder T J 2015 Robust calibration of a universal single-qubit gate set via robust phase estimation *Phys. Rev.* A **92** 062315
[29] Supplemental material. Includes details about the statistical uncertainty in phase estimations, interferometry method C, control of the trap stiffness in our experimental system, an algorithm for analysing the results of the binary search algorithm, and evolution of the state vector during the pulse sequences.
[30] Lindberg A 2020 Improving the coherent quantum control of trapped ion qubits *Master thesis* Stockholm University
[31] Ma L-S, Jungner P, Ye J and Hall J L 1994 Delivering the same optical frequency at two places: accurate cancellation of phase noise introduced by an optical fiber or other time-varying path *Opt. Lett.* **19** 1777–9
[32] Huber T, Lambrecht A, Schmidt J, Karpa L and Schaetz T 2014 A far-off-resonance optical trap for a Ba^{+} ion *Nat. Commun.* **5** 5587
[33] Rudinger K, Kimmel S, Lobser D and Maunz P 2017 Experimental demonstration of a cheap and accurate phase estimation *Phys. Rev. Lett.* **118** 190502
[34] Home J P, Hanneke D, Jost J D, Amini J M, Leibfried D and Wineland D J 2009 Complete methods set for scalable ion trap quantum information processing *Science* **325** 1227–30
[35] Guggemos M 2017 Precision spectroscopy with trapped $^{40}Ca^{+}$ and $^{27}Al^{+}$ ions *PhD thesis* Universität Innsbruck
[36] Dubé P, Madej A A, Tibbo M and Bernard J E 2014 High-accuracy measurement of the differential scalar polarizability of a $^{88}Sr^{+}$ clock using the time-dilation effect *Phys. Rev. Lett.* **112** 173002
[37] Boixo S and Somma R D 2008 Parameter estimation with mixed-state quantum computation *Phys. Rev.* A **77** 052320
[38] Higgins B L, Berry D W, Bartlett S D, Wiseman H M and Pryde G J 2007 Entanglement-free Heisenberg-limited phase estimation *Nature* **450** 393–6
[39] Pham P T T 2005 A general-purpose pulse sequencer for quantum computing *Master thesis* Massachusetts Institute of Technology
[40] Schindler P 2008 Frequency synthesis and pulse shaping for quantum information processing with trapped ions *Master thesis* Universität Innsbruck
[41] Heinrich D 2020 Ultrafast coherent excitation of a $^{40}Ca^{+}$ ion *PhD thesis* Universität Innsbruck
[42] Higgins B L, Berry D W, Bartlett S D, Mitchell M W, Wiseman H M and Pryde G J 2009 Demonstrating Heisenberg-limited unambiguous phase estimation without adaptive measurements *New J. Phys.* **11** 073023
[43] Giovannetti V, Lloyd S and Maccone L 2004 Quantum-enhanced measurements: beating the standard quantum limit *Science* **306** 1330–6
[44] Roos C 2000 Controlling the quantum state of trapped ions *PhD thesis* Universität Innsbruck
[45] Herschbach N, Pyka K, Keller J and Mehlstäubler T E 2012 Linear Paul trap design for an optical clock with Coulomb crystals *Appl. Phys.* B **107** 891–906
[46] Pyka K, Herschbach N, Keller J and Mehlstäubler T E 2014 A high-precision segmented Paul trap with minimized micromotion for an optical multiple-ion clock *Appl. Phys.* B **114** 231–41
[47] Keller J, Kalincev D, Burgermeister T, Kulosa A P, Didier A, Nordmann T, Kiethe J and Mehlstäubler T E 2019 Probing time dilation in Coulomb crystals in a high-precision ion trap *Phys. Rev. Appl.* **11** 011002
[48] Bartlett S D, Rudolph T and Spekkens R W 2007 Reference frames, superselection rules, and quantum information *Rev. Mod. Phys.* **79** 555–609
[49] Eddington A S 1924 *The Mathematical Theory of Relativity* 2nd edn (Cambridge: Cambridge University Press)
[50] Brewer S M, Chen J S, Hankin A M, Clements E R, Chou C W, Wineland D J, Hume D B and Leibrandt D R 2019 $^{27}Al^{+}$ quantum-logic clock with a systematic uncertainty below 10^{-18} *Phys. Rev. Lett.* **123** 033201
[51] Sterk J D, Luo L, Manning T A, Maunz P and Monroe C 2012 Photon collection from a trapped ion-cavity system *Phys. Rev.* A **85** 062308
[52] Steiner M, Meyer H M, Deutsch C, Reichel J and Köhl M 2013 Single ion coupled to an optical fiber cavity *Phys. Rev. Lett.* **110** 043003
[53] Stute A, Casabone B, Brandstätter B, Friebe K, Northup T E and Blatt R 2013 Quantum-state transfer from an ion to a photon *Nat. Photon.* **7** 219–22
[54] Brown K R, Ospelkaus C, Colombe Y, Wilson A C, Leibfried D and Wineland D J 2011 Coupled quantized mechanical oscillators *Nature* **471** 196–9
[55] Harlander M, Lechner R, Brownnutt M, Blatt R and Hänsel W 2011 Trapped-ion antennae for the transmission of quantum information *Nature* **471** 200–3
[56] Wilson A C, Colombe Y, Brown K R, Knill E, Leibfried D and Wineland D J 2014 Tunable spin-spin interactions and entanglement of ions in separate potential wells *Nature* **512** 57–60
[57] Kumph M, Holz P, Langer K, Meraner M, Niedermayr M, Brownnutt M and Blatt R 2016 Operation of a planar-electrode ion-trap array with adjustable RF electrodes *New J. Phys.* **18** 023047
[58] Mehta K K, Zhang C, Malinowski M, Nguyen T-L, Stadler M and Home J P 2020 Integrated optical multi-ion quantum logic *Nature* **586** 533–7
[59] Niffenegger R J *et al* 2020 Integrated multi-wavelength control of an ion qubit *Nature* **586** 538–42
[60] Champenois C, Marciante M, Pedregosa-Gutierrez J, Houssin M, Knoop M and Kajita M 2010 Ion ring in a linear multipole trap for optical frequency metrology *Phys. Rev.* A **81** 043410
[61] Arnold K, Hajiyev E, Paez E, Lee C H, Barrett M D and Bollinger J 2015 Prospects for atomic clocks based on large ion crystals *Phys. Rev.* A **92** 032108
[62] Gilmore K A, Affolter M, Lewis-Swan R J, Barberena D, Jordan E, Rey A M and Bollinger J J 2021 Quantum-enhanced sensing of displacements and electric fields with two-dimensional trapped-ion crystals *Science* **373** 673–8

[63] Chen J S 2017 Ticking near the zero-point energy: towards 1×10^{-18} accuracy in Al^{+} optical clocks *PhD thesis* University of Colorado, Boulder
[64] Kotler S, Akerman N, Glickman Y, Keselman A and Ozeri R 2011 Single-ion quantum lock-in amplifier *Nature* **473** 61–5
[65] Macalpine W and Schildknecht R 1959 Coaxial resonators with helical inner conductor *Proc. IRE* **47** 2099–105
[66] Siverns J D, Simkins L R, Weidt S and Hensinger W K 2012 On the application of radio frequency voltages to ion traps via helical resonators *Appl. Phys.* B **107** 921–34
[67] Hempel C 2014 Digital quantum simulation, Schrödinger cat state spectroscopy and setting up a linear ion trap *PhD thesis* Universität Innsbruck
[68] Johnson K G, Wong-Campos J D, Restelli A, Landsman K A, Neyenhuis B, Mizrahi J and Monroe C 2016 Active stabilization of ion trap radiofrequency potentials *Rev. Sci. Instrum.* **87** 053110
[69] Brandl M 2017 Towards cryogenic scalable quantum computing with trapped ions *PhD thesis* Universität Innsbruck
[70] Neuhaus L, Metzdorff R, Chua S, Jacqmin T, Briant T, Heidmann A, Cohadon P F and Deléglise S 2017 PyRPL (Python Red Pitaya Lockbox)—an open-source software package for FPGA-controlled quantum optics experiments *2017 European Conf. Lasers and Electro-Optics and European Quantum Electronics Conf.* (Optical Society of America)
[71] Neuhaus L 2016 *PyRPL Develop-0.9.3. GitHub* (https://github.com/lneuhaus/pyrpl/tree/develop-0.9.3) (accessed 30 January 2021)
[72] Meier A M, Burkhardt K A, McMahon B J and Herold C D 2019 Testing the robustness of robust phase estimation *Phys. Rev.* A **100** 052106